

PAPER • OPEN ACCESS

Cobalt nickel boride as electrocatalyst for the oxidation of alcohols in alkaline media

To cite this article: Michael Braun *et al* 2023 *J. Phys. Energy* **5** 024005

View the [article online](#) for updates and enhancements.

You may also like

- [Effect of Silver Modification on Glycerol Oxidation Reaction Activity of Palladium Electrode in Alkaline Medium](#)
Hiroshi Inoue, Yuki Teraoka, Masanobu Chiku *et al.*
- [Effect of Defective Graphene Flake for Catalysts of Supported Pd Nanocubes toward Glucose Oxidation Reaction in Alkaline Medium](#)
Bang-De Hong, Kung-Lung Hunag, Ho-Rei Chen *et al.*
- [Structural, optical and electrical properties of ribbon-like graphene oxide thin films](#)
T H T Aziz and M M Salleh



PAPER

OPEN ACCESS

RECEIVED

7 October 2022

REVISED

1 February 2023

ACCEPTED FOR PUBLICATION

10 February 2023

PUBLISHED

2 March 2023

Original content from this work may be used under the terms of the [Creative Commons Attribution 4.0 licence](https://creativecommons.org/licenses/by/4.0/).

Any further distribution of this work must maintain attribution to the author(s) and the title of the work, journal citation and DOI.



Cobalt nickel boride as electrocatalyst for the oxidation of alcohols in alkaline media

Michael Braun¹ , Mohit Chatwani^{1,2} , Piyush Kumar^{1,2} , Yun Hao¹ , Ignacio Sanjuán¹ , Ariadni-Aikaterini Apostoleri³ , Ann Cathrin Brix³ , Dulce M Morales^{3,4} , Ulrich Hagemann⁵ , Markus Heidelmann⁵ , Justus Masa⁶ , Wolfgang Schuhmann³ and Corina Andronescu^{1,*}

¹ Chemical Technology III, Faculty of Chemistry and CENIDE, Center for Nanointegration, University of Duisburg-Essen, Carl-Benz-Straße 199, 47057 Duisburg, Germany

² Indian Institute of Science Education and Research (IISER), Dr Homi Bhabha Road, Pune 411008, India

³ Analytical Chemistry, Center for Electrochemical Sciences (CES), Ruhr University Bochum, Universitätsstr. 150, 44801 Bochum, Germany

⁴ Chemical Engineering group, Engineering and Technology Institute Groningen (ENTEG), Nijenborgh 4, Groningen, 9747 AG, The Netherlands

⁵ Interdisciplinary Center for Analytics on the Nanoscale (ICAN) and CENIDE, Center for Nanointegration Duisburg-Essen, NanoEnergieTechnikZentrum at University of Duisburg-Essen Carl-Benz-Straße 199, 47057 Duisburg, Germany

⁶ Max-Planck-Institute for Chemical Energy Conversion (MPI-CEC), Stiftstraße 34-36, 45470 Mülheim an der Ruhr, Germany

* Author to whom any correspondence should be addressed.

E-mail: corina.andronescu@uni-due.de

Keywords: alcohol electrooxidation, ionomer, rotating disk electrode, flow cell

Supplementary material for this article is available [online](#)

Abstract

A mixed Co and Ni boride precursor was synthesized via chemical reduction and subsequently annealed at 400 or 500 °C with or without prior addition of the monomer benzoxazine (BO). The resulting mixed CoNiB materials were investigated as electrocatalysts for three alcohol oxidation reactions (AOR) in alkaline electrolyte: the oxidation of glycerol (GOR), ethylene glycol (EGOR) and ethanol (EOR). Comparison of the rotating disk electrode (RDE) cyclic voltammograms for the different catalysts revealed that CoNiB annealed at 500 °C without the addition of BO exhibited the lowest overpotentials in AORs at 10 mA cm⁻², promoting GOR at 224 ± 6 mV lower potential compared to OER. When pyrolysis was conducted at 400 °C, the BO-containing catalyst showed a significant increase in the electrocatalytic activity for the AORs compared to the CoNiB catalyst only. The product selectivity on the different catalysts was investigated in a batch-type reactor with flow recirculation revealing formate as the main oxidation product during GOR and EGOR with faradaic efficiencies (FE) in a range of 60%–80%, while acetate was obtained during EOR (FE ~ 85%–90%). The electrode potential, electrolyte composition and the type of ionomer were explored with respect to their influence on the GOR selectivity. The use of different ionomers resulted in significant differences in the activity trends between RDE and the batch-type reactor with flow recirculation measurements, indicating a strong influence of the two different substrates used, namely glassy carbon and carbon paper on the catalyst formation and thus on the recorded electrochemical activity.

1. Introduction

In light of the increase in the atmospheric CO₂ concentration, the rise of the global temperature and the impact of climate change, replacing a fossil fuel-based economy with one based on renewable energy is vital. The sources of green energy such as wind and sunlight could then not only be used for the provision of electrical energy but also to directly produce basic chemicals and fuels. Electrocatalysis, which is precisely at the junction between electrical and chemical energy, will play a central role in accomplishing this task [1–3].

The electrochemical splitting of water produces hydrogen and oxygen at the cathode and the anode, respectively. Hydrogen has the potential to emerge as a future energy carrier and fuel that can be stored, burned, refined, or used as a replacement for other fossil fuel-based reducing agents such as coke, for example in the steel industry [4, 5]. Nevertheless, the necessary electrical energy to drive the electrolytic processes must come from green energy sources in order to achieve the goal of net-zero CO₂ emissions. In addition, to facilitate water electrolysis on an industrially relevant scale, an efficient process and thus also cost-effective electrocatalysts are necessary [6, 7]. Since the electrochemical oxygen evolution reaction (OER) requires the transfer of four protons coupled to four electrons, while in the electrochemical hydrogen evolution reaction only two protons coupled to two electrons are needed, OER is the kinetically limiting reaction in water electrolysis showing typically slower kinetics and consequently also higher overpotentials [8]. Alternative anode reactions such as the oxidation of alcohols (AOR) offer the possibility to use less electrical energy and generate value-added products, thereby improving the overall energy and cost efficiency of the electrolytic process [9–11]. Small chain alcohols can be used as inexpensive and readily available sustainable feedstocks because they can also be produced from biomass [12, 13]. Glycerol, for example, is a by-product of biodiesel production, which is obtained via the transesterification of vegetable oils [12, 14]. Glycerol can be oxidized into numerous valuable chemicals used in many different industries. The potential products include formic acid/formate, which can be utilized as a fuel in fuel cells, as an anti-icing agent and as a food or rubber additive [15, 16]. The market price of formic acid (85 wt.%) was around 0.6–0.8 \$ per kg [17] in 2019, whereas glycerol (80 wt.%) cost about 0.08–0.18 \$ per kg [18] in the same year. Thus, by converting glycerol to formic acid, a potential four- to seven-fold value increase can be achieved.

Mono- or polymetallic catalysts containing precious metals such as Ru [19, 20], Pd [21, 22], Pt [23, 24], or Au [25, 26] have been successfully tested for the AOR and the electrochemical glycerol oxidation reaction (GOR) in particular. Although these materials show low overpotentials, they have several drawbacks concerning their use at an industrial scale, as precious metals are scarce and expensive, meanwhile low current densities are often obtained due to the formation of an oxide layer *in situ* or CO-poisoning. In contrast, 3d transition metals are earth-abundant, low-priced, stable under alkaline conditions and enable higher current densities, albeit at higher potentials compared to the noble metal-based catalysts. In the AOR, catalyst materials especially based on Ni and/or Co as their respective metals and metallic nanoparticles [27, 28], layered double hydroxides [29, 30], hydroxides [31, 32], spinels [33–37], perovskites [38, 39] or other oxide materials [40–42] are commonly used. Additionally, Ni-based borides were shown to catalyze the oxidation of alcohols such as methanol [43], solketal [44], HMF [45] and glycerol [46, 47] as well.

As it is known from OER research, the combination of Co and Ni is an attractive pathway to enhance the activity of the corresponding monometallic Co or Ni borides [48–53]. A Co_{0.1}Ni_{0.9}B catalyst synthesized via chemical reduction [48] allowed 10 mA cm⁻² to be recorded at a considerably lower overpotential (η_{10}) of only 330 mV compared to the monometallic Co and Ni borides. Similarly, Xu *et al* [49] obtained a CoNiB catalyst on Ni foam (NF) after chemical reduction and annealing at 500 °C, which revealed a higher activity than the as-prepared CoNiB@NF (without the annealing step), Co_xB@NF and the noble metal-based RuO₂ at current densities of 50 mA cm⁻². Moreover, Sun *et al* [50] prepared CoNiB nanosheets by chemical reduction followed by annealing at 400 °C and found superior activity of CoNiB over Co_xB and Ni_xB with a η_{10} value of 320 mV. To our knowledge, the application of mixed Co and Ni borides for electrocatalysis of the GOR, EGOR and EOR has not yet been reported.

The pyrolysis of polybenzoxazines, which can be formed by thermal polymerization of benzoxazine (BO) monomers, can generate an amorphous carbon matrix into which catalyst materials can be embedded. Furthermore, the carbon matrix can provide additional electrical conductivity as well as stability of the catalyst film, which has been demonstrated for different electrocatalytic reactions such as the OER [54–57], the oxygen reduction reaction (ORR) [57], and the carbon dioxide reduction reaction (CO₂RR) [58].

In this study, a mixed Co and Ni boride (CoNiB) composite was synthesized by chemical reduction. The obtained precursor was subsequently annealed at 400/500 °C in an inert gas atmosphere to form the active catalyst material. Furthermore, the addition of a BO monomer to the catalyst was explored and the respective influence on the catalyst activity and selectivity for the GOR, EGOR and EOR was investigated using cyclic voltammetry in a rotating disk electrode (RDE) setup and chronoamperometry in a batch-type reactor under flow recirculation. Furthermore, the influence of the electrode potential, electrolyte composition and the ionomer used for the preparation of the catalyst film on the selectivity during GOR was investigated.

2. Methods

2.1. Materials

Co(II) chloride, anhydrous (Sigma-Aldrich, >97%), Ni(II) chloride hexahydrate (Sigma-Aldrich, 99.9%), sodium borohydride (Sigma-Aldrich, >98.0%), glycerol (Fisher Scientific, ≥99%), ethylene glycol (Acros

Organics, 99%), absolute ethanol (VWR International, 99.97%), acetone (Sigma-Aldrich, >99.5%), Nafion (Sigma-Aldrich, 5 wt.% in lower aliphatic alcohols and water, 0.93 mg ml⁻¹), Sustainion (Dioxide Materials, 5 wt.% in ethanol, 0.79 mg ml⁻¹), Ni-foam (Goodfellow), BO (Huntsman, Araldite MT 35 600 CH), NaOH (Sigma-Aldrich, >97.0%), sulfuric acid (Merck, 98%), ammonium formate (Sigma-Aldrich, ≥99%), glycolic acid (Sigma-Aldrich, 99%), calcium L-(–)-glycerate dihydrate (Alfa Aesar) and oxalic acid (Fluorochem) were used as purchased without further purification. KOH solutions (Fisher Scientific, 86.8%) were purified by a Chelex 100 cation-exchange resin (Sigma-Aldrich, 50–100 mesh) to remove metal impurities. All solutions were prepared with ultrapure water.

2.2. Synthesis

The CoNiB precursor was prepared in a round-bottomed flask in which 25 ml of an aqueous solution of both 1 M cobalt chloride and 1 M nickel chloride was deaerated, flushed with argon and kept at 0 °C using an ice bath. A syringe was used to slowly inject deaerated 1 M sodium borohydride in 0.1 M NaOH into the metal salt solution [59, 60]. The precipitate of the prepared borides was collected and washed with considerable volumes of ultrapure water and ethanol and further stored in acetone. To synthesize the catalyst materials, the precursor was dried under an inert gas stream and either directly transferred to a ceramic boat to perform the heat treatment procedure or was dispersed in EtOH (5 mg ml⁻¹) to which BO was added in a mass ratio of precursor to BO of 7:1. The dispersion was sonicated in an ultrasonic bath for 15 min and the solvent was evaporated at room temperature in an inert gas stream. The powder was transferred to a ceramic boat and the following pyrolysis procedure was performed in a tube furnace: The temperature was increased to 200 °C and kept for 2 h, followed by a second temperature increase to either 400 or 500 °C where the temperature was held for 2 h. A heating ramp of 10 °C min⁻¹ and an Ar flow of 100 ml min⁻¹ were used throughout the thermal treatment.

2.3. Characterization

2.3.1. Structural characterization

Powder x-ray diffraction (PXRD) patterns were recorded at room temperature using Cu K α radiation on a Bruker D8 Discover x-ray diffractometer in reflection mode ($2\theta = 30^\circ$ – 80° , step size 0.01°). For data treatment and evaluation, the Bruker software DIFFRAC.EVA was used.

Inductively coupled plasma–mass spectrometry (ICP-MS) measurements were performed with an Anton Paar Multiwave PRO. For the measurement, 10 mg of sample were dissolved in concentrated nitric acid and diluted with water.

Scanning electron microscopy (SEM) and energy-dispersive x-ray spectroscopy (EDX) measurements were recorded using a Quanta 3D FEG scanning electron microscope (FEI) operated at 20 kV along with EDX using 30 kV accelerating voltages.

X-ray photoelectron spectroscopy (XPS) measurements were performed using a VersaProbe II (ULVAC-Phi 5000) with a monochromatic Al K α source. Reported sensitivity factors [61] were corrected for the specific transmission of the instrument by a transmission function, which was calculated by measuring the different Cu peaks on a sputter-cleaned Cu foil, deriving thus machine-specific sensitivity factors. The software used for fitting was CasaXPS. Quantitative atomic concentrations and analyses of the species were performed for the B 1s, C 1s and O 1s photoemission peaks. Due to potential inaccuracies resulting from the Ni LMM contributions to the Co 2p signals, atomic concentrations of Co and Ni were calculated from the 3p spectra, while the deconvolution of the Co and Ni species was performed on the 2p_{3/2} signals accounting for the Ni LMM peak. To obtain an estimate of the Ni LMM intensity, the Ni LMM and Ni 3p combination of a Co-free sample was analyzed beforehand.

Transmission electron microscopy (TEM) measurements were carried out on a Jeol JEM 2200 fs microscope (Akishima, Japan) equipped with a probe-side Cs corrector operated at 200 kV acceleration voltage. The images were taken in conventional bright field mode. EDX elemental mappings were acquired with an X-Max 100 detector (Oxford Instruments, Abingdon, United Kingdom).

Contact Angle Measurements were performed using OCA15PRO equipment (Data Physics Instruments GmbH).

2.3.2. Electrochemical characterization

2.3.2.1. Electrocatalytic activity

The electrochemical measurements were performed using a Metrohm Autolab bipotentiostat/galvanostat PGSTAT302N in an RDE three-electrode setup. As electrolyte, either Ar-saturated 1 M KOH solution or Ar-saturated 1 M KOH + 0.1 M alcohol (ethanol, ethylene glycol or glycerol) was used. As a working electrode (WE) a glassy carbon disc (0.113 cm² geometric area) was used, while a platinum coil and a double junction Ag/AgCl (3 M KCl) electrode were used as counter (CE) and reference electrodes (RE), respectively.

Catalyst inks of 5 mg ml⁻¹ were prepared in a mixture of ultrapure water, ethanol and Nafion solution (volumetric ratio of 49:49:2) and sonicated for 15 min. When Sustainion was tested the volumetric ratio of water, ethanol and ionomer was adjusted to a ratio of 48.8:48.8:2.3. 6.78 μl of the respective ink was drop-casted on the polished glassy carbon RDE and dried at room temperature to obtain a catalyst mass loading of 300 μg cm⁻². Electrochemical impedance spectra (EIS) were collected at open-circuit potential (OCP) to determine the uncompensated resistance in a frequency range of 100 kHz to 0.1 kHz using a 10 mV (RMS) AC amplitude. Cyclic voltammograms were recorded from 0 to 0.8 V vs. Ag/AgCl (3 M KCl) using a scan rate of 5 mV s⁻¹ at a rotation speed of 1600 rpm. Three consecutive cyclic voltammograms were obtained. For each catalyst, all the measurements were conducted in triplicate. The recorded potentials were converted from Ag/AgCl (3 M KCl) scale to the reversible hydrogen electrode (RHE) scale using equations (1) and (2).

$$E_{\text{RHE}} = E_{\text{measured}} + E_{\text{Ag/AgCl (3 M KCl)}}^0 + 0.059\text{pH} - i \cdot R_U \quad (1)$$

$$\text{pH} = 14 + \log([\text{OH}^-]) + \log(\gamma) \quad (2)$$

E_{RHE} : WE potential vs. RHE, E_{measured} : Measured potential at the WE vs. Ag/AgCl (3 M KCl), $E_{\text{Ag/AgCl (3 M KCl)}}^0$: Formal potential of Ag/AgCl (3 M KCl) vs. RHE, pH: pH value determined considering the OH⁻ concentration and using an average value of $\gamma = 0.766$ [62–64] for the activity coefficient of KOH in water (see equation (2)), i : Measured current, R_U : Uncompensated resistance.

2.3.2.2. Determination of the electrochemical double-layer capacitance

The electrochemical double-layer capacitance (C_{dl}) was determined in the already described three-electrode RDE setup using Ar-saturated 1 M KOH. Ten cyclic voltammograms were recorded in a 500 mV window in the non-faradaic potential region of -0.1 to -0.6 V vs. Ag/AgCl (3 M KCl) using different scan rates (ν): 0.01, 0.05, 0.1, 0.25, 0.5, 0.75, 1, 2.5, 5, 7.5, 10, 12.5 and 15 V s⁻¹. The double-layer charging current (i_c) was extracted from the last anodic scans at the center potential of -0.35 V and plotted against the scan rate (ν). The electrochemical double-layer capacitance was obtained by fitting to an allometric model using equation (3) as previously described elsewhere [65]. The range of the scan rates used for the respective fitting of double-layer charging currents was optimized for each catalyst and the corresponding C_{dl} value was then used as an estimation for the ECSA since a proportional relationship is widely accepted [66].

$$i_c = C_{\text{dl}} \cdot \nu^b \quad (3)$$

2.3.2.3. Electrolysis in a batch-type reactor with flow recirculation

Chronoamperometric measurements (CA) were performed in a batch-type reactor with flow recirculation (abbreviated as flow cell) containing two compartments separated by an anion exchange membrane (Fumatech fumasep FAA-3-PK-130). Ni-foam was used as a counter electrode in the cathode compartment, while in the anode compartment the catalyst-modified carbon paper (H23, Freudenberg, 0.95 cm² geometric area exposed to electrolyte) and an Ag/AgCl (3.4 M KCl) leak-free reference electrode (Innovative Instruments, Inc.) were used as WE and RE, respectively. 1 M KOH solution was introduced in the cathode compartment, while in the anode compartment 0.1 M alcohol (glycerol, ethylene glycol, or ethanol) in 1 M KOH was used at a constant flow rate of 7 ml min⁻¹. Catalyst-modified carbon paper electrodes were prepared by spray-coating. The powder catalysts were dispersed in a 0.2 vol.% solution of Nafion in ethanol or 0.23 vol.% solution of Sustainion in ethanol to generate catalyst inks with a concentration of 1.3 mg ml⁻¹. The spray-coating process was performed while heating the carbon support at 125 °C and a mass loading close to 0.5 mg cm⁻² was obtained. Measurements were conducted using Metrohm Autolab bipotentiostat/galvanostat PGSTAT302N or PGSTAT204. Impedance spectra were collected as described before and the CA measurements were carried out at 0.5 V vs. Ag/AgCl (3.4 M KCl) for 4 h.

2.3.2.4. Product analysis

250 μl of a sample was collected manually at different reaction times (1, 2, 3 and 4 h) from both anodic and cathodic compartments. The samples were diluted with 300 μl of 0.5 M H₂SO₄ directly after sampling and before performing high-performance liquid chromatography (HPLC) measurements. Measurements were conducted on the AZURA HPLC system (Knauer) with a refractive index detector (RID 2.1 l, Knauer) and a diode array detector (UV/VIS, DAD 2.1 l, Knauer). An ion-exclusion column (Eurokat H, Knauer) and precolumn were used at 70 °C and a flow rate of 0.6 ml min⁻¹ with 5 mM H₂SO₄ as the eluent to separate the products obtained from AOR. Products were assigned by calibration with commercially available reference compounds. The products were measured by the UV/Vis detector at 220 nm. Since glycerol and formic acid

overlap in the refractive index detector (RID), glycerol concentrations were calculated as described previously [67]. The Faradaic efficiency (FE) was calculated using equation (4) and averaged over two electrodes per potential and catalyst [36].

$$\text{Faradaic efficiency} = \frac{1}{\nu_p} \cdot \frac{(n_{t,\text{product}} - n_{i,\text{product}}) \cdot F \cdot n(e^-)}{Q_{\text{total}}} \cdot 100\% \quad (4)$$

ν_p	Stoichiometric factor,
$n_{t,\text{product}}$	Number of moles of the respective product at time t in mol,
$n_{i,\text{product}}$	Initial number of moles of the respective product in mol,
F	Faraday's constant; 96 485 C mol ⁻¹ ,
$n(e^-)$	Number of electrons from the oxidation of 1 mol of glycerol into the respective product in mol,
Q_{total}	Total charge passed WE during electrolysis in C.

2.3.2.5. Differential electrochemical mass spectrometry (DEMS)

Experiments were conducted using a Hidden HPR40 DEMS system (Hidden Analytical Ltd, UK). An electron energy of 70 eV was used for ionization with an emission current of 500 μA . Ionized oxygen ($m/z = 32$) was accelerated with a voltage of 3 V and detected by a Faraday Cup detector. Electrochemistry during DEMS experiments was performed on a Biologic VSP-300 potentiostat in a single-compartment thin-layer cell made of PEEK with a three-electrode configuration (supplied by HIDDEN Analytical Ltd.). Cyclic voltammograms were recorded from +1 to +1.8 V vs. RHE at a scan rate of 2 mV s⁻¹. The electrolyte was circulated through the cell in a continuous flow mode with a rate of 60 $\mu\text{l min}^{-1}$ by means of a syringe pump. The WE was a glassy carbon rod of 5 mm diameter with the catalyst drop-coated on top with a loading of 0.3 mg cm⁻². The counter electrode was a Pt wire of 0.5 mm diameter set at the outlet of the electrolyte and the reference electrode was a leakless Ag/AgCl (3.4 M KCl) reference electrode (Innovative Instruments, Inc., USA). A 28 μm thick PTFE membrane with a pore size of 20 nm was located between the thin-layer cell and the mass spectrometer inlet port. DEMS signals were processed to minimize the influence of bubble noise on the recorded trends with the smoothing method 'Averaging adjacent' between 3–5 points using the software 'Origin Pro 2020'. DEMS signals shown are background subtracted.

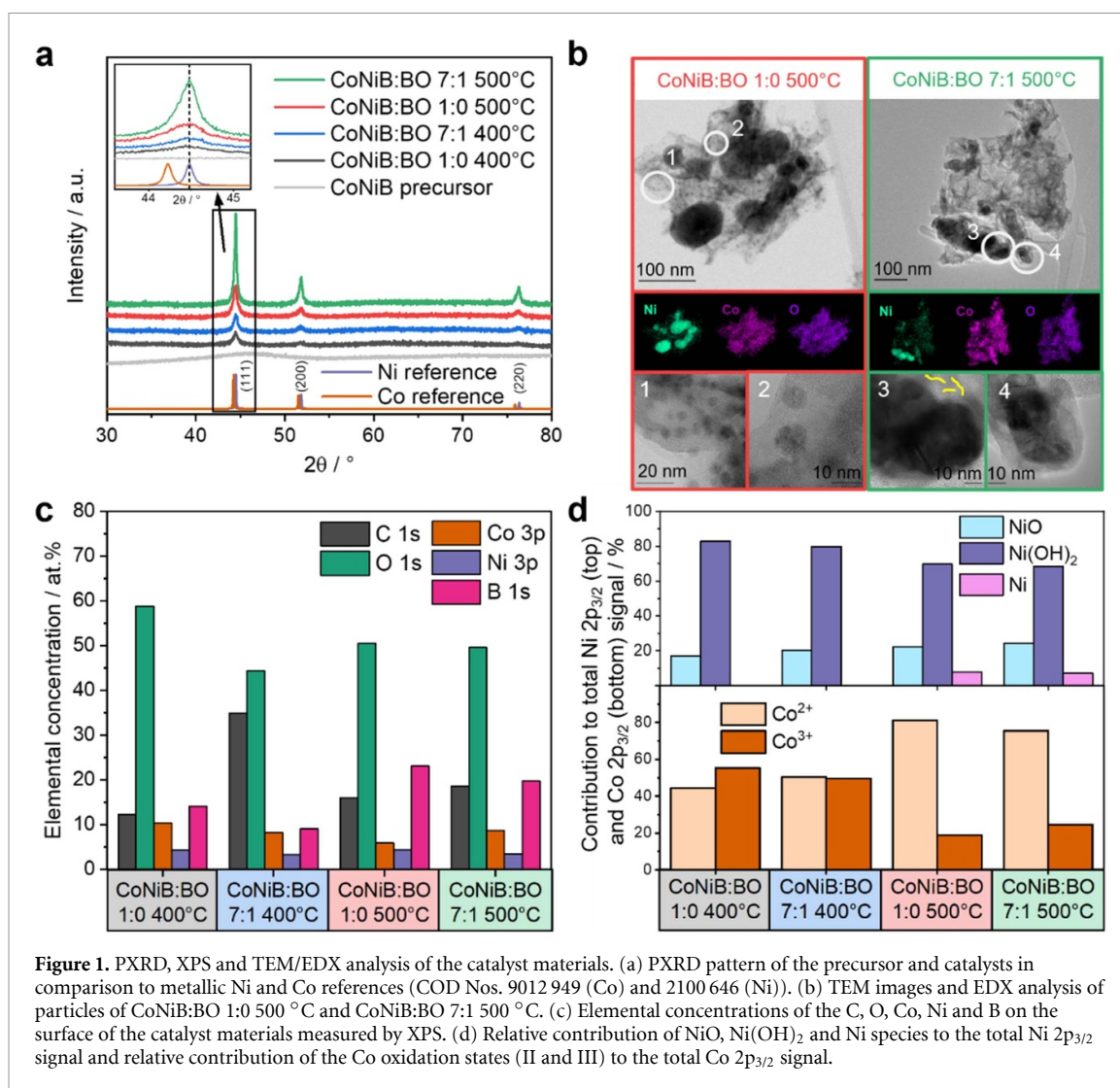
The calibration of the m/z 32 DEMS signals and the corresponding O₂ faradaic current densities (j_{Oxygen}) was conducted with a reported active and stable OER catalyst, a Co-hydroxynitrate [68], in an alcohol-free 1 M KOH solution. The following expression was found:

$$j_{\text{Oxygen}} \text{ (mAcm}^{-2}\text{)} = m/z \text{ 32 DEMS signal (Torr)} \cdot 7.56887 \times 10^9 \quad (5)$$

3. Results and discussion

The CoNiB precursor was synthesized by chemical reduction of Co and Ni chloride salts with NaBH₄ in 0.1 M NaOH. Inductively coupled plasma–mass spectrometry (ICP-MS) revealed a Co:Ni:B ratio of 1.0:1.1:1.1 in the final material. The CoNiB precursor was either dispersed in BO-containing EtOH at a mass ratio of precursor:BO of 7:1, which was found to be the most promising in preliminary experiments (figure S1) or used as prepared and pyrolyzed at 400/500 °C in Ar atmosphere. The resulting samples are labeled with the CoNiB precursor:BO ratio and the pyrolysis temperature, e.g. 'CoNiB:BO 1:0 500 °C' for the CoNiB catalyst that was not mixed with BO, annealed at 500 °C.

Scanning electron microscopy (SEM) images of the CoNiB materials are presented in figure S2. The catalysts do not show clearly defined morphologies. While the BO-free catalysts (1:0) seem to have a more 3D appearance, the BO-containing materials (7:1) seem to be more platelet- and 2D-like. Slight differences in the crystalline structure were identified based on the PXRD patterns shown in figure 1(a). For the precursor, only a broad diffraction signal at around $2\theta = 45^\circ$ can be noticed, which reflects its x-ray amorphous structure and is consistent with other reports on Co and Ni borides formed via chemical reduction by NaBH₄ [48, 49, 53, 69]. On the other hand, the catalyst materials reveal the presence of metallic Ni reflections with possible small contributions of metallic Co, whereas other crystalline phases cannot be identified. The most intense reflection at $2\theta = 44.5^\circ$, present in all diffractograms, is assigned to the metallic Ni (111) plane. Its intensity increases strongly when higher temperatures are used during the pyrolysis step and when BO has been added to the CoNiB precursor. The occurrence of metallic Ni can be attributed to the unusual metal-metalloid structure, in which nanocrystalline metal clusters are embedded in an amorphous B-based matrix consisting of B(OH)₃, B₂O₃ and metal borides that supposedly prevent the metallic cores from their growth and oxidation [49, 69, 70]. Here, the thermal treatment may have led to a crystallization of the formerly x-ray



amorphous Ni core, which was further enhanced by the addition of a reductive carbon source such as BO and was most pronounced at 500 °C. The formation of crystalline domains within an amorphous matrix can also be observed at different magnifications of the TEM images of particles from CoNiB:BO 1:0 500 °C and 7:1 500 °C in figure 1(b). Furthermore, Ni appears to aggregate more strongly than Co and O, as indicated by the EDX analyses of the catalyst particles (figure 1(b)). Moreover, the 1:0 samples show several small crystalline subregions with a diameter of <10 nm (figure 1(b)—region 2), which are observed less frequently in the BO-containing catalyst, for which regions of layers with a distance of 3.4 Å can be noticed (marked in yellow), attributed to graphitic carbon formed most probably via the pyrolysis of the C precursor BO.

The materials were further characterized by XPS and the corresponding spectra and their deconvolution are displayed in figure S3, while a summary of the elemental concentration of the respective elements and the type of the Ni and Co species is provided in figures 1(c) and (d) and table S1. The dominant element on the surface of the catalyst is O, which is present in Ni or Co hydroxides (531.3 eV) and as surface organic oxygen (532.2 eV) [51, 71]. Higher C contents manifested on the surface when BO was added to the CoNiB precursor prior to the pyrolysis step. The presence of carbon in the BO-free catalysts could be associated with adventitious carbon and the contact of the material with ethanol and acetone during the washing and storage of the sample, respectively. The B concentration is higher for the samples pyrolyzed at 500 °C ranging between 20–25 at.%, while only 8–14 at.% was observed when pyrolysis was conducted at 400 °C with the highest relative B content on the surface found for CoNiB:BO 1:0 500 °C. In the B 1s spectra, it can be noted that the binding energy lies at 192.0 (400 °C) and 192.6 eV (500 °C), respectively, which was previously reported for oxidized B species [59, 60, 72]. The positive shift in the binding energy of the B 1s level at 400 °C and 500 °C may indicate a change in the electronic properties on the surface induced by the pyrolysis process. In the B 1s spectrum, an interaction of Ni and Co with B can be observed typically at lower binding energies (~187.7 eV), while its absence is in alignment with previous reports [49, 50, 60].

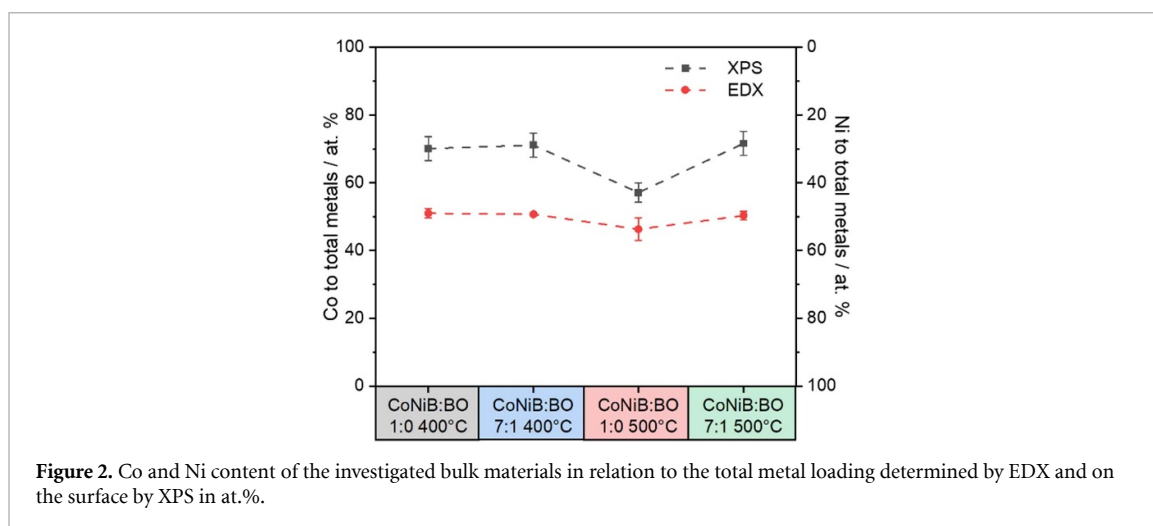


Figure S3(e) shows the high-resolution XPS spectra of Ni 2p. The characteristic Ni 2p_{3/2} core peak appears at 855.2 eV for the pyrolyzed samples at 400 °C. For those prepared at 500 °C, the Ni 2p_{3/2} core peak is shifted positively towards higher binding energies at 855.6 eV, indicating a possible loss of electron density from Ni. The Ni 2p spectra of the samples pyrolyzed at 400 °C and 500 °C suggest that Ni at the surface is predominantly in the oxidation state of +II as the signals could be deconvoluted into Ni(OH)₂ and NiO [71]. For the samples pyrolyzed at 500 °C, minor contributions of Ni⁰ (figures 2(d) and S3(e)) can be noticed, which agrees with the more intense reflections of metallic Ni in the PXRD measurements (figure 1(a)). At 400 °C, the main Ni species on the surface of the samples is Ni(OH)₂, while at 500 °C an increased amount of NiO was noted (figure 1(d)), suggesting the loss of water molecules from Ni(OH)₂ at higher pyrolysis temperatures.

The core peak of the Co 2p_{3/2} level (figure S3(d)) is found at 780.5 eV (400 °C) and 781.5 eV (500 °C), corresponding to a Co oxidation state of +II (mainly from CoO and Co(OH)₂) and +III (MgCo₂O₄ [73] was used as reference). The Auger peak of Ni LMM was also considered in the deconvolution of the Co 2p spectrum [61]. The positive chemical shift of the Co 2p_{3/2} levels at higher pyrolysis temperatures indicates modulation of the electron density at the metal Co, being previously observed when annealing Co₃B over a temperature range of 200–800 °C [74]. The appearance of both surface Ni and Co hydroxides/oxides can be attributed to the formation of a core–shell structure by spontaneous surface oxidation from air and water exposure [59]. In the case of Co, at a pyrolysis temperature of 400 °C, both Co²⁺ and Co³⁺ contribute equally to the Co 2p_{3/2} signal, while a pyrolysis temperature of 500 °C leads to a higher concentration of Co²⁺ on the surface, which is visible by the more pronounced satellite peak in the Co 2p spectra (figure 1(d)).

Interestingly, the Co concentration determined by XPS in relation to the total metal loading was higher on the surface with ~70 at.% for most of the catalysts, while on CoNiB:BO 1:0 500 °C it reached only 57 at.%. On the other hand, EDX analysis of the bulk materials resulted in Co:Ni ratios of around 50:50 (figure 2 and table S2), which is consistent with the nominal metal ratio during the chemical reduction reaction and the ICP-MS results for the precursor composition. Furthermore, like the XPS results, the EDX results also show a lower Co to the total metal content in CoNiB:BO 1:0 500 °C, indicating not only a surface effect. Consequently, the XPS and EDX results suggest a dynamic situation during the annealing/pyrolysis process as the segregation of B causes the Ni and Co concentrations on the surface to decline, usually leaving higher concentrations of Co than Ni.

The CoNiB-based materials were drop-casted on polished glassy carbon (GC) electrodes and their electrocatalytic activity towards the OER, GOR, EGOR and EOR was investigated by recording three consecutive cyclic voltammograms (CV) in Ar-saturated 1 M KOH or 1 M KOH + 0.1 M of the respective alcohol (glycerol, ethylene glycol, or ethanol) with an RDE setup. The first CVs obtained using the different catalysts are presented in figure 3, while the second and third CVs are depicted in figures S4–S7. In the case of the OER, the CoNiB-based materials show similar activity with a η_{10} of 330 ± 2 , 321 ± 1 , 309 ± 1 , and 324 ± 1 mV for CoNiB:BO 1:0 400 °C, CoNiB:BO 7:1 400 °C, CoNiB:BO 1:0 500 °C and CoNiB:BO 7:1 500 °C, respectively (table S3 and figure S8). While CoNiB:BO 1:0 500 °C is the most active catalyst in the OER, CoNiB:BO 1:0 400 °C is the least active, which becomes even more evident at higher overpotentials. Additionally, an oxidation peak can be observed at around 1.1–1.2 V vs. RHE that could be assigned to the Co(OH)₂/CoOOH transition and can also be noticed in the different alcohol-containing electrolytes in figure 3.

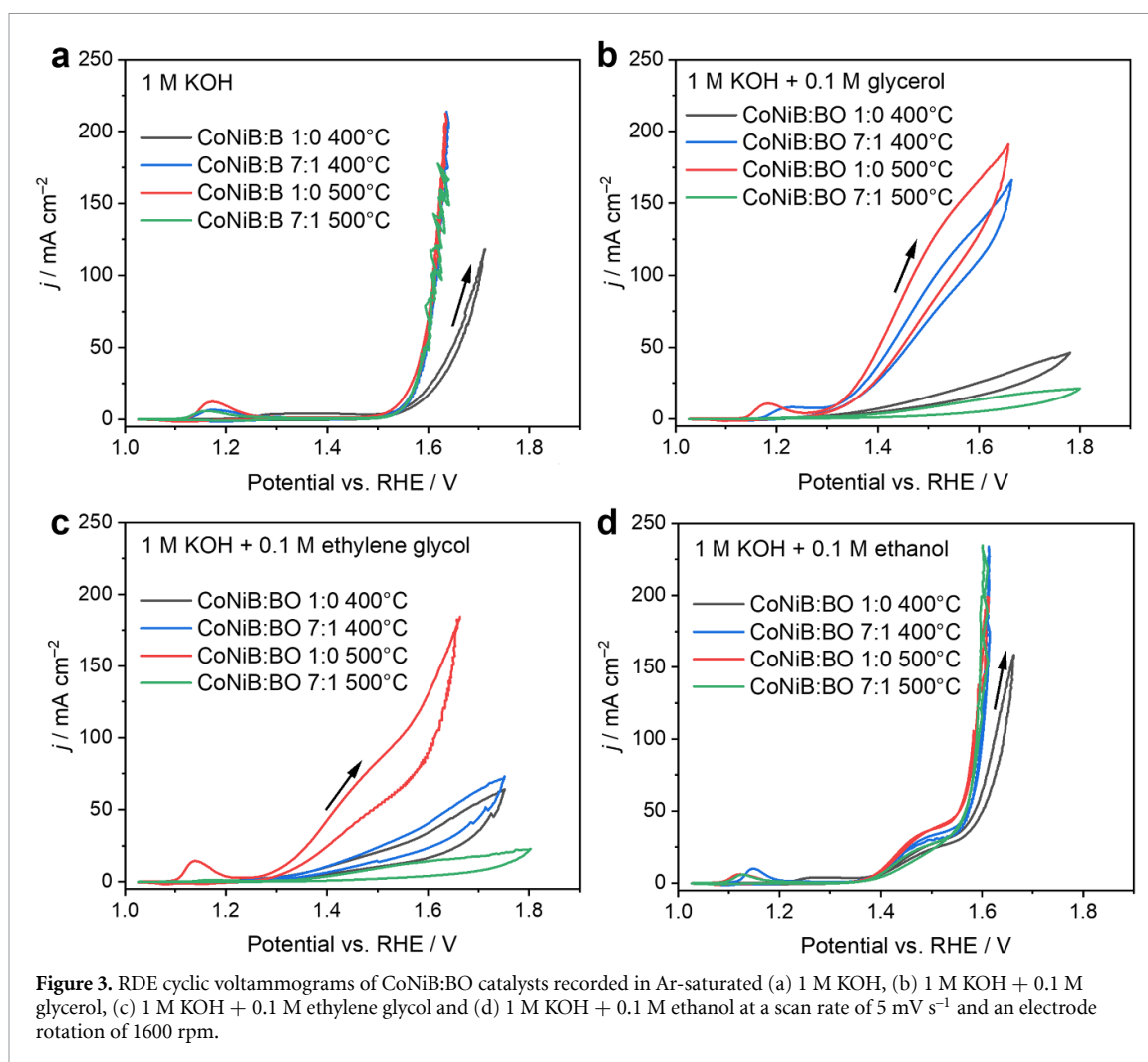


Figure 3. RDE cyclic voltammograms of CoNiB:BO catalysts recorded in Ar-saturated (a) 1 M KOH, (b) 1 M KOH + 0.1 M glycerol, (c) 1 M KOH + 0.1 M ethylene glycol and (d) 1 M KOH + 0.1 M ethanol at a scan rate of 5 mV s^{-1} and an electrode rotation of 1600 rpm.

When 0.1 M glycerol was added to the KOH electrolyte (figure 3(b)), the shape of the cyclic voltammograms (CVs) as well as the activity trend changed. While in 1 M KOH-only solution, the currents increase exponentially at potentials $>1.5 \text{ V}$ vs. RHE, in the alcohol-containing electrolyte the current increase is observed at much lower potentials without the same sharp increase at around 1.5 V vs. RHE. DEMS measurements confirm that the OER is suppressed in the glycerol-containing electrolyte using CoNiB:BO 1:0 500 °C as a model catalyst, with oxygen being detected at potentials $>1.55 \text{ V}$ vs. RHE (figure S9). Furthermore, the currents recorded in the cathodic scans of the CVs are smaller compared to the anodic scans for all four catalysts and the electrocatalytic activity during the successive CVs slightly decreases (figures S4–S7), indicating deactivation processes resulting from surface blockage due to strongly adsorbed intermediates and/or catalyst instability also influenced by the high upper limit potential of the CV [38, 67]. Similar to the results obtained in the alcohol-free 1 M KOH, CoNiB:BO 1:0 500 °C is the most active catalyst in 1 M KOH + 0.1 M glycerol, with 10 mA cm^{-2} current density recorded at 1.32 V vs. RHE. The second most active catalyst is CoNiB:BO 7:1 400 °C, which requires $\sim 10 \text{ mV}$ more to reach the same current density, followed by CoNiB:BO 1:0 400 °C and CoNiB:BO 7:1 500 °C with 1.44 V and 1.54 V vs. RHE, respectively. The potential difference between E_{OER} and E_{GOR} ($\Delta\eta_{\text{OER-AOR}}$) to reach the mentioned current density corresponds to the saved energy by substituting the OER with an alternative anode reaction such as the GOR, with $224 \pm 6 \text{ mV}$ for the most active GOR catalyst, CoNiB:BO 1:0 500 °C (table S4 and figure S10).

Figure 3(c) depicts the CVs in 1 M KOH + 0.1 M ethylene glycol and the activity trend in generating 10 mA cm^{-2} follows the same trend as the one found in 1 M KOH + 0.1 M glycerol, namely: CoNiB:BO 1:0 500 °C (1.31 V vs. RHE) $>$ CoNiB:BO 7:1 400 °C (1.38 V vs. RHE) $>$ CoNiB:BO 1:0 400 °C (1.40 V vs. RHE) $>$ CoNiB:BO 7:1 400 °C (1.54 V vs. RHE). In contrast to the glycerol-containing electrolyte, the anodic currents increase with a higher slope at potentials of $>1.5 \text{ V}$ vs. RHE, indicating a stronger contribution from the OER; as confirmed by DEMS measurements (figure S9). The maximum energy saved by replacing the OER with the EGOR is $230 \pm 2 \text{ mV}$ realized with CoNiB:BO 1:0 500 °C. The similarity of

the activity trend in the two alcohol-containing electrolytes may be related to the fact that both investigated alcohols so far are vicinal alcohols.

Similar to the GOR and EGOR, in the presence of 0.1 M ethanol in 1 M KOH CoNiB:BO 1:0 500 °C is the most active catalyst with 1.40 V vs. RHE to achieve 10 mA cm⁻². The activity of CoNiB:BO 7:1 500 °C shows higher EOR activity compared to the other AOR, with similar electrocatalytic activity (1.44 V vs. RHE) as CoNiB:BO 7:1 400 °C (1.42 V vs. RHE), and CoNiB:BO 1:0 400 °C (1.45 V vs. RHE) (figure 3(d)). For EOR, the currents begin to rise at ~1.4 V vs. RHE and reach a plateau at 1.5 V vs. RHE before increasing more strongly at 1.6 V vs. RHE, where O₂ starts to be evolved, as shown by DEMS (figure S9).

While in 1 M KOH the catalysts show only small differences in the recorded currents, the thermal treatment of the CoNiB precursor at 500 °C without the addition of BO seems to result in a catalyst with clearly beneficial activity for the AOR. In comparison, lower currents are obtained for the corresponding CoNiB:BO 1:0 catalyst treated at 400 °C. Nevertheless, the addition of BO before the pyrolysis at 400 °C results in a significantly increased electrocatalytic activity, with CoNiB:BO 7:1 400 °C being the second most active catalyst in all the alcohol-containing electrolytes. At a potential of 1.50 V vs. RHE, where only little contributions from the OER are expected, as shown by the DEMS measurements (figure S9), the current density achieved on CoNiB:BO 7:1 400 °C is higher in all reactions compared to the CoNiB:BO 1:0 400 °C (figure S11). However, a similar boost in the activity could not be observed when BO was added to the CoNiB precursor and heated at 500 °C. In fact, the activity of CoNiB:BO 7:1 500 °C is always lower compared to the BO-free catalysts.

To gain further insight into the activity trends of the investigated reactions and particularly the high electrocatalytic activity of the CoNiB:BO 1:0 500 °C catalyst, we determined the double layer capacitance (C_{dl}) as a proportional measure for the electrocatalytic surface area (ECSA) of the different catalysts in 1 M KOH by CV (figure S12 and table S5) [66]. It was found that the C_{dl} values of the four catalysts are similar, ranging between 14.8–23.4 μF. CoNiB:BO 1:0 500 °C, which displays the highest activity for the four reactions, exhibits the lowest C_{dl} value (14.8 μF) and thus the lowest ECSA of the different catalysts. In addition, CoNiB:BO 1:0 400 °C, for which the highest C_{dl} value (23.4 μF) was obtained, turned out to be one of the least active catalysts for the OER and AOR. Based on this, it can be inferred that the observed activities of the CoNiB:BO samples cannot be solely explained by their surface area, but they are also related to their intrinsic catalytic activity.

It appears that the position and the intensity of the Co²⁺/Co³⁺ oxidation peak depend on the catalyst as well as on the alcohol present in the electrolyte (figure S13). It is well known that in the case of Ni-containing catalysts, the redox conversion is always visible and well defined, while in the case of Co this is not the case. Similar changes were reported for mixed Co and Ni borides, for which a shift of the peak towards positive potential was observed with increased Ni content [53]. In 1 M KOH, the most active OER electrocatalysts, CoNiB:BO 1:0 500 °C, shows the most pronounced peak in the 1.1–1.2 V vs. RHE potential window. Interestingly, the redox conversion of the catalyst surface seems to be dependent on the investigated alcohol (figure S14). While in ethanol, the peak shifts towards more cathodic potential, the presence of glycerol seems to delay the surface oxidation process and a peak shifts towards anodic potentials is observed. It can be hypothesized that the dependence of the Co(II) oxidation potential in the presence of different alcohols is due to the formation of different adsorption configurations of the alcohols at the active sites.

During the AOR, valuable products can be obtained. To investigate product selectivity, the different CoNiB-based electrocatalysts were spray-coated on a carbon paper used as WEs in a batch-type reactor with flow recirculation, abbreviated as a 'flow cell' (figure S15). Electrolysis was performed for 4 h at a constant potential of 1.52 V vs. RHE (figure 4) using alcohol-containing electrolyte (1 M KOH + 0.1 M alcohol) as anolyte and 1 M KOH solution as catholyte. Samples of the electrolytes were collected each hour and the AOR products were measured using high-performance liquid chromatography (HPLC). The products were detected in the form of organic acids but are reported here in their conjugate base form due to the high pH of the electrolyte during the reaction. Representative chromatograms from CoNiB:BO 1:0 500 °C are presented in figure S16 and the concentration profiles depending on the electrolysis time are shown in figures S17–S19.

The resulting chronoamperometric measurements are displayed in figures 4(a),(c), and (e), whereas the corresponding FEs are shown in figures 4(b), (d) and (f). The recorded currents all follow a similar profile. A sharp decrease in the currents is observed at the beginning, followed by a less pronounced decrease after 30 min caused by the reactants' continuous depletion. The detected products in the electrooxidation of 1 M KOH + 0.1 M glycerol are formate with FEs in the range of 70%–80%, glycolate (FE of 4%–7%), and glycerate (FE < 1%), while in 1 M KOH + 0.1 M ethylene glycol predominantly formate (FE of 60%–75%) and glycolate (FE of 1%–4%) are formed. Small amounts of oxalate can be detected in both cases. In contrast, only acetate was detected in 1 M KOH + 0.1 M ethanol with FEs in the range of 85%–90%. These results are consistent with reports of the selectivity of other Co and Ni-based non-noble metal catalysts in the AOR [40–42, 46, 75]. The overall FEs during the AOR experiments do not reach 100%, indicating that

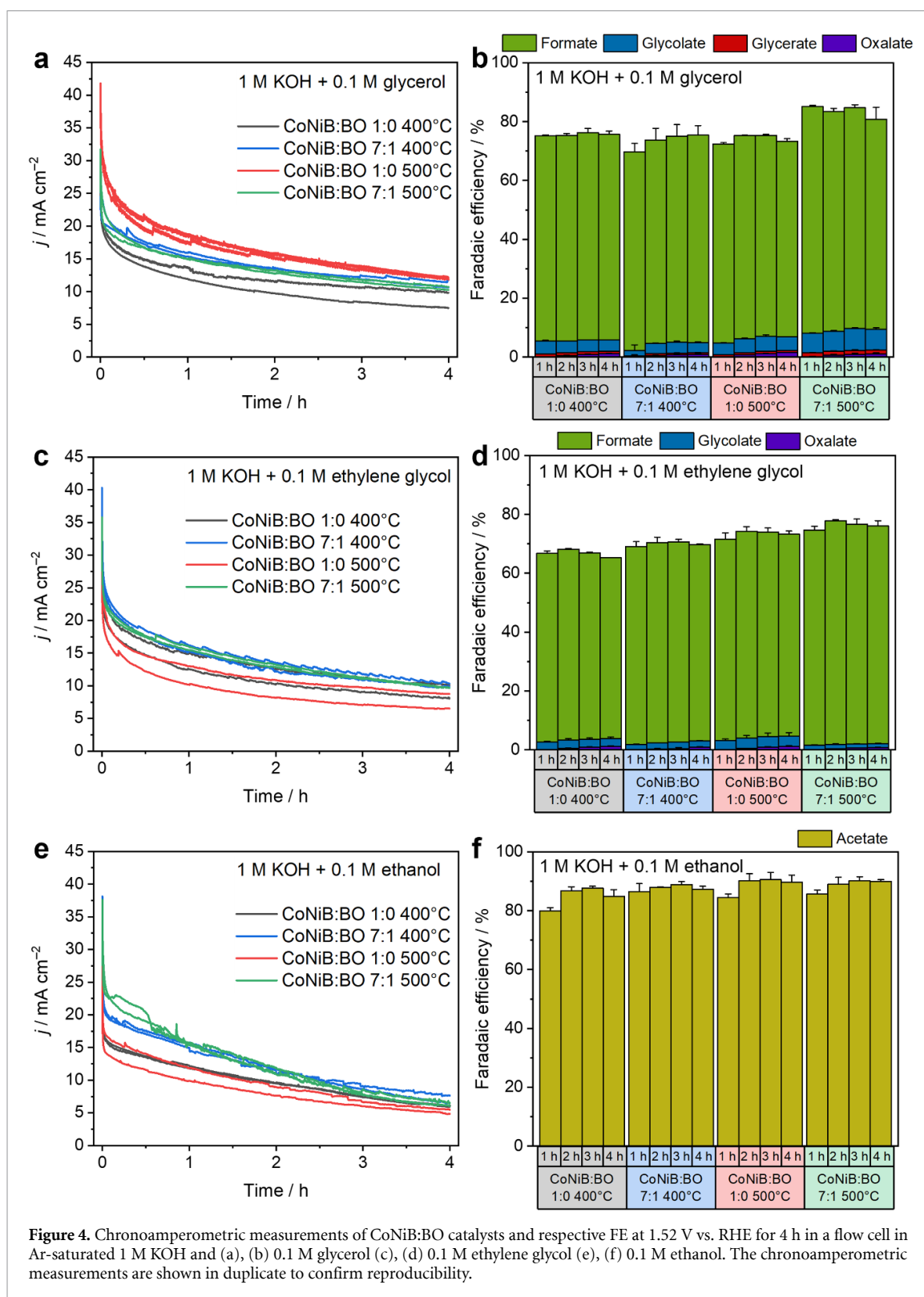
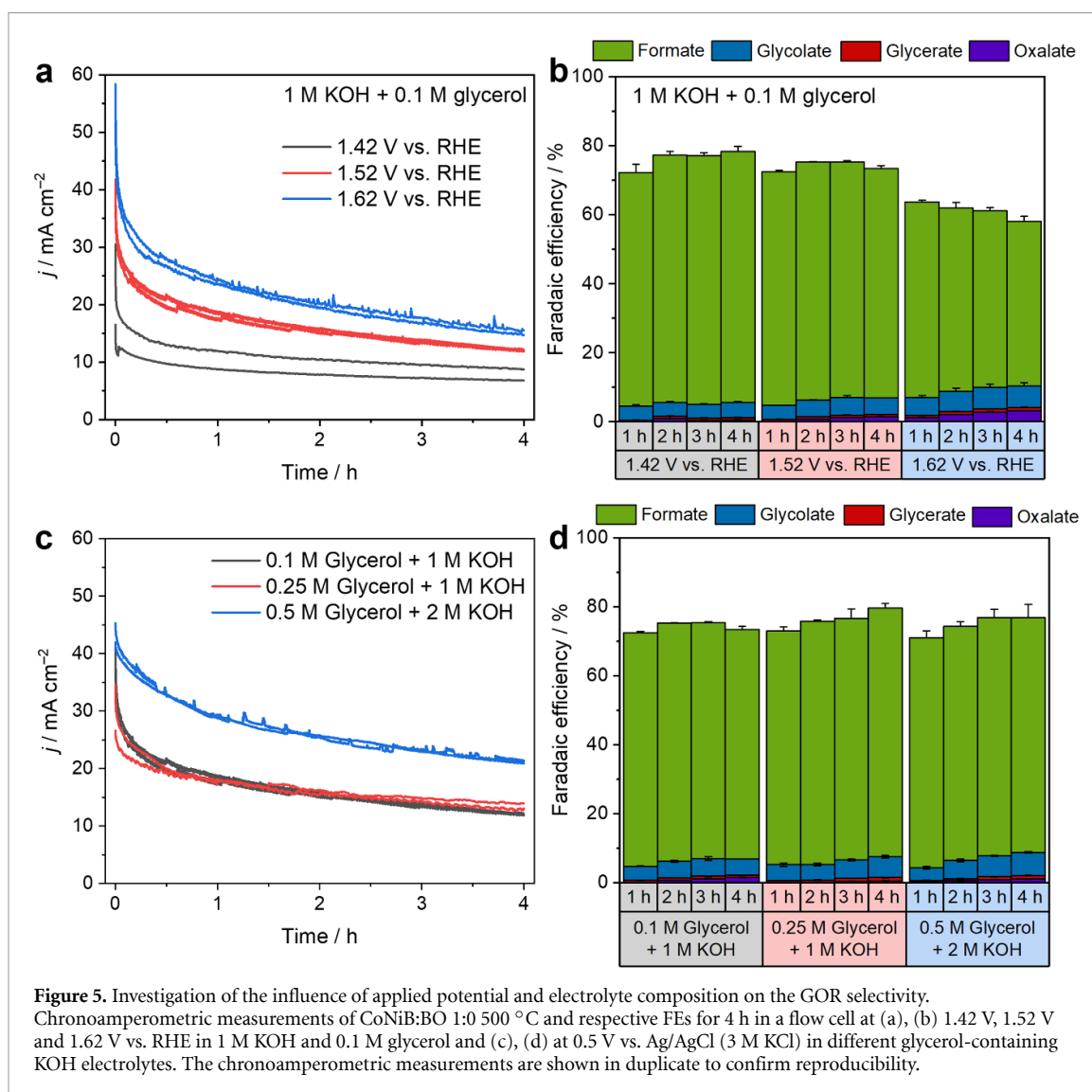


Figure 4. Chronoamperometric measurements of CoNiB:BO catalysts and respective FE at 1.52 V vs. RHE for 4 h in a flow cell in Ar-saturated 1 M KOH and (a), (b) 0.1 M glycerol (c), (d) 0.1 M ethylene glycol (e), (f) 0.1 M ethanol. The chronoamperometric measurements are shown in duplicate to confirm reproducibility.

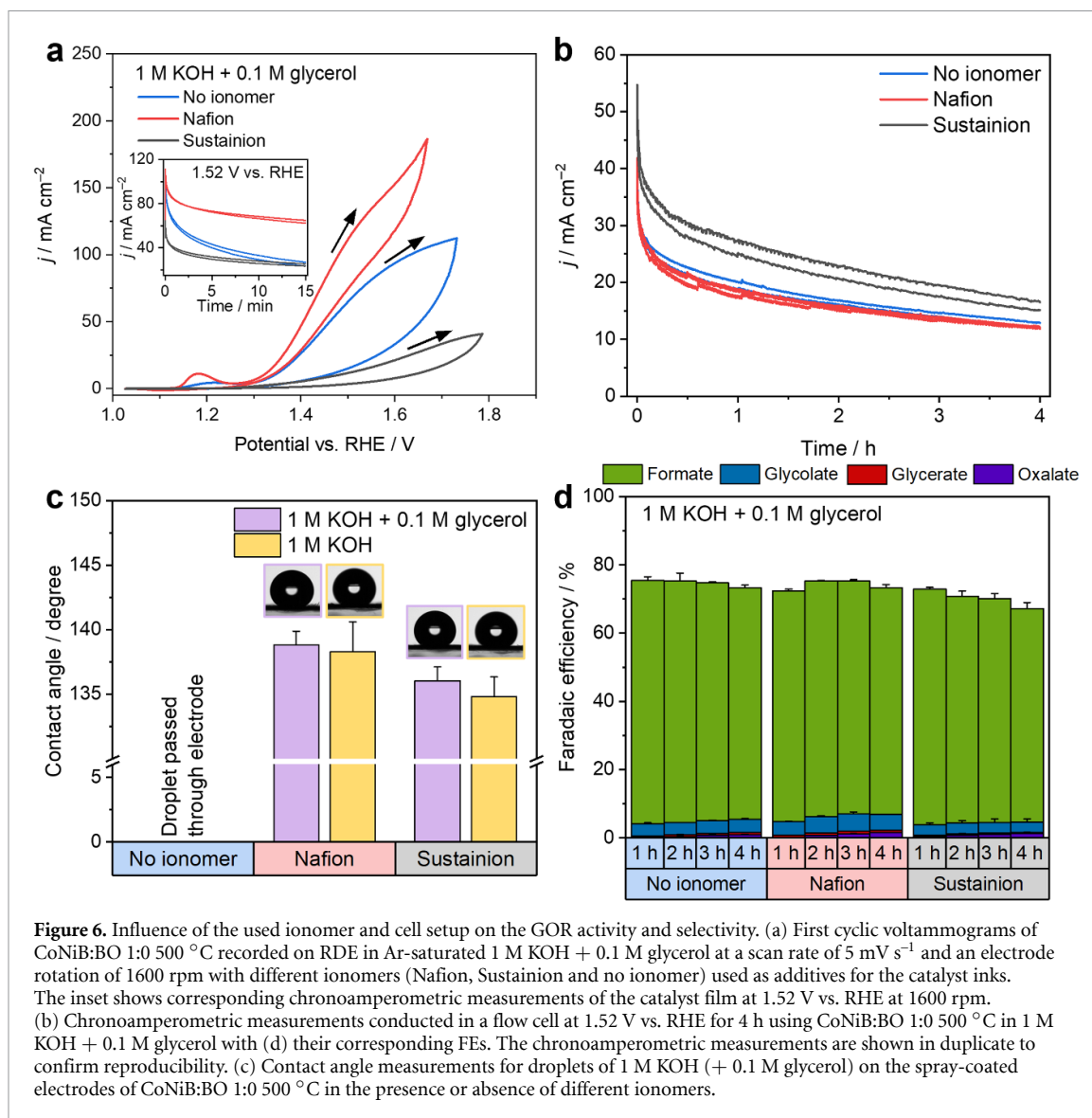
further oxidation to CO₂ may occur, which we cannot detect due to the CO₂ conversion to carbonate. In addition, oxygen may be formed at the anode but at this potential, the contribution of the competing OER to the recorded currents, and thus to the FE, is expected to be small as illustrated by the DEMS measurements (figure S9).

Interestingly, despite the different electrocatalytic activities obtained in the RDE experiments, FEs during the AOR are similar for all catalysts and do not change significantly with the electrolysis time, suggesting that the different pyrolysis temperatures and the addition of BO during the Co and Ni boride catalyst synthesis do not influence the AOR selectivity strongly. Additionally, it can be observed that the activity trends in the RDE experiments are not equally reflected in the flow cell measurements, as CoNiB:BO 1:0 500 °C, for example,



reaches the highest currents in 1 M KOH + 0.1 M glycerol in both the RDE and flow cell experiments but shows the lowest currents on average during EGOR and EOR in comparison to the other boride catalysts in the flow cell measurements. Furthermore, the BO-containing catalyst offered higher current densities than the BO-free catalysts during the flow cell measurements, unlike in the RDE experiments. This discrepancy between the RDE and flow cell measurements could partly be attributed to the different experimental conditions. While for the flow cell measurements, a three-dimensional WE of $\sim 1 \text{ cm}^2$ (catalyst loading: 0.5 mg cm^{-2}) is prepared by spray-coating of the respective catalyst and 7 ml of electrolyte are circulated in the anodic half-cell at a flow rate of 7 ml min^{-1} for several hours, for the RDE experiments the catalyst inks are drop-casted on a two-dimensional glassy carbon electrode with $\sim 0.1 \text{ cm}^2$ (catalyst loading: 0.3 mg cm^{-2}), which is rotated at 1600 rpm in 100 ml of electrolyte for several minutes. Thus, for example, the concentration of intermediates and products may differ over time and differences in the mass transport may also occur owing to the different measurement setups and catalyst films. On the one hand, these results emphasize that the two systems may not be exactly comparable, but on the other hand they underline the importance of measuring electrocatalytic performances of these boride materials not only via RDE but also using a setup that resembles more closely those used for industrial applications.

To investigate the influence of the potential and electrolyte composition on the GOR selectivity, we used CoNiB:BO 1:0 500 °C as a representative catalyst and the resulting chronoamperometric measurements and the corresponding FEs are shown in figure 5. Additionally, the obtained concentration profiles are depicted in figures S20 and S21. When electrolysis was conducted at a potential of 1.42 V vs. RHE, the total FEs were higher than those obtained at 1.52 V vs. RHE. At 1.62 V vs. RHE we observed an even further decrease in the total FE for the valuable glycerol products (except CO_2 or carbonate), most probably due to an increased formation of O_2 at this potential or even CO_2 formation as a result of the higher driving force. In addition,



higher potentials favor higher FEs for the formation of oxalate, which has also been found by Morales *et al* [40] during GOR on NiO_x nanoparticles.

Brix *et al* [46] reported that on solid state-synthesized Ni boride the concentration of the C3-product lactate was highest when 2 M KOH and 0.5 M glycerol (KOH:glycerol ratio of 4:1) were used as electrolyte. The same KOH:glycerol ratios in 1 and 2 M KOH was also explored here to favor the formation of C3-products (figures 5(c) and (d)). While the currents increase noticeably in 2 M KOH + 0.5 M glycerol in comparison to the previously tested 1 M KOH + 0.1 M glycerol, using only a higher concentration of the reactant glycerol in 1 M KOH did not alter the recorded currents, which can be ascribed to the lower ion mobility in a more viscous electrolyte [42, 46]. However, the selectivity of the GOR did not change significantly using a different electrolyte composition and formate is still the main product next to small amounts of glycolate and glycerate.

Polyalcohols such as glycerol can be deprotonated in strongly alkaline solutions to form alcoholate anions [67, 76] which may impact their transport towards the electrode surface. Ionomers are usually introduced as electrode additives to enable proton or OH⁻ transport and improve the mechanical stability of the electrode films. While this is extensively explored in other fields, such as CO₂ electroreduction to modulate the catalyst microenvironment, such strategies are not used extensively in AOR [77, 78]. Therefore, in this work we explored an anion- and a cation-conducting ionomer during GOR on CoNiB-based electrodes (figure S22). We expected that the positive charges from the imidazolium constituents in the Sustainion ionomer could attract both glycerolate and hydroxide ions and consequently provide increased glycerol and OH⁻ transport to the catalyst surface. CoNiB:BO 1:0 500 °C was used as catalyst and the results are shown in figure 6. Using RDE cyclic voltammetry, we observed a significant impact of the additive on the recorded current density. For the Nafion-containing electrode, an increased current density is recorded, while for the

Sustainion-containing electrode lower current densities are attained compared with the ionomer-free catalyst film. The same activity trend was obtained when chronoamperometric measurements at 1.52 V vs. RHE were performed in the RDE setup (figure 6(a) inset). Similarly, when the measurements were carried out in 1 M KOH, 1 M KOH + 0.1 M ethylene glycol, and 1 M KOH + 0.1 M ethanol considering the current at 1.5 V vs. RHE, the same order can be observed (figure S23). Li *et al* [78] also observed the same order in activity during OER using IrO₂ in an RDE setup with Nafion as the cation-conducting and AS-4 (Tokuyama Corp.) as the anion-conducting ionomer. The different types of ionomers in the catalyst inks may have led to changes in the catalyst film and thus to the accessibility of the active sites, so we assessed the double-layer capacitance (C_{dl}) of the different films (table S6). When Sustainion is used as an ionomer the C_{dl} reaches the highest value of 27 μ F, while using Nafion gives only 15 μ F. This suggests that the use of Sustainion creates catalyst films with a higher ECSA than Nafion on the RDE. Therefore, the lower activity of the Sustainion-based catalyst film does not result from a potentially lower number of active sites but could be the result of a more complex interaction between the catalyst, the ionomer, the current collector, and the anodic reaction under investigation. As we investigated the electrodes prepared by the different catalyst inks in the flow cell, the activity order for the GOR is reversed: Sustainion > no ionomer > Nafion, although the difference between ionomer-free electrode and the one containing Nafion is not as pronounced as in the RDE measurements (figure 6(b)). SEM images (figure S24) confirm that the addition of Sustainion in the catalyst ink leads to the formation of a more homogeneous film on the carbon fibers with a few micrometer-sized catalyst agglomerates, while Nafion inks seem to cause more agglomeration and form less homogeneously coated electrodes. This effect could explain the lower current densities obtained using Nafion-containing inks since active sites on or inside the catalyst agglomerates might not be in contact with the electrolyte or in contact with the conductive substrate and might thus not take part in the reaction.

Another parameter that may impact the recorded current is the wettability of the catalyst film. Contact angle measurements (figure 6(c)) show that the addition of Sustainion and Nafion in the catalyst layer increased the hydrophobicity with similar contact angles around 135°–140° for both cases. The values do not show high variation when using 1 M KOH or 1 M KOH + 0.1 M glycerol. The results from the contact angle measurements do not indicate a correlation of the recorded currents with the hydrophobicity of the electrode. Moreover, the selectivity during the GOR seems to be purely defined by the catalyst and is not influenced by the ionomer, as similar FEs were recorded on the electrodes prepared with Nafion, Sustainion, or in the absence of any ionomer (figures 6(d) and S25).

To further understand the reason behind the different observed activity trends, cut-out areas from the carbon paper sheets spray-coated with CoNiB:BO 1:0 500 °C in the presence of different ionomers were glued onto an RDE and both chronoamperometric as well as CVs were performed (figure S26). The results show that the activity trend of the spray-coated electrodes in the RDE setup resembles the one observed during the flow cell measurements (figure 6(b)). As a result, the different measurement setups yield the same trend with the same electrode substrates, indicating their strong influence on the activity trend. So, we assume that the different surface functionalities presented in the support materials may lead to different catalyst film formations on the electrode. This is influenced by the different interactions between the catalyst/ionomer aggregates from the dispersion ink, leading to the observable differences in activity trends, as already reported for fuel cells [79–81].

4. Conclusion

Four different mixed Co and Ni boride catalyst materials were prepared from a boride precursor by annealing at 400 or 500 °C with or without the addition of BO as a carbon precursor. The borides were shown to be active electrocatalysts for the OER as well as for alternative anode reactions such as GOR, EGOR and EOR. Among the four catalysts, CoNiB:BO 1:0 500 °C was found to be the most active electrocatalyst in all the tested reactions. Moreover, it was discovered that the addition of BO could enhance the electrocatalytic activity of CoNiB pyrolyzed at 400 °C for the alcohol oxidation reactions at a potential of 1.50 V vs. RHE.

Although very different activities in terms of current densities and overpotentials were obtained for the catalysts using RDE, flow cell measurements revealed high product selectivities that were similar for all four catalysts. In the case of GOR and EGOR, formate, a valuable C1 compound, was the main product generated with FEs in the range of 60%–80%, whereas acetate was primarily formed during EOR with FEs of 85%–90%. Different activity trends were observed in the flow cell measurements compared to the RDE, depending on the alcohol used during the experiment. While during GOR, the highest currents in the flow cell measurements were recorded on CoNiB:BO 1:0 500 °C, for EGOR and EOR, the BO-containing catalysts allowed for a higher current to be recorded.

Using CoNiB:BO 1:0 500 °C as a representative catalyst material, possible influences on the selectivity of the GOR, such as the working electrode potential, the electrolyte composition and the ionomer used as an

additive for the preparation of the catalyst film, were investigated. It could be shown that the electrode potentials and electrolyte compositions tested here lead to minor changes in selectivity. Surprisingly, it was found out that the type of ionomer can strongly influence the electrocatalytic activity without influencing the GOR selectivity. In addition, significant differences in activity trends were observed between the RDE and flow cell measurements for which the preparation of the catalyst films with the borides on two different substrates, namely glassy carbon and carbon paper, may be responsible. These findings suggest that quickly and widely accessible RDE measurements alone may not be a conclusive determinant of the electrocatalytic activity of the Co and Ni borides prepared in this study and that more application-oriented methods, such as the flow cell measurements will be of great benefit in properly evaluating their electrocatalytic activity for the AOR. In addition, further engineering of the catalyst layers depending on the current collector may be used to promote AOR conversion.

Data availability statement

The data that support the findings of this study are available upon reasonable request from the authors.

Acknowledgments

We gratefully acknowledge the Deutsche Forschungsgemeinschaft (DFG, German Research Foundation) for funding through the research group FOR 2982 ‘UNusual anODE reactions in electrochemical energy conversion: Value creation rather than oxygen evolution in hydrogen production (UNODE)’ (Project Numbers 433304702 C A, 433304666 W S). Vimanshu Chanda, Simon Schumacher and Sabine Seisel are acknowledged for the contact angle measurements, SEM images, EDX and PXRD measurements at the Ruhr-University Bochum. C A acknowledges the Mercator Research Center Ruhr (MERCUR.Exzellenz, ‘DIMENSION’ Ex-2021-0034).

Conflict of interest

There are no conflicts of interest to declare.

ORCID iDs

Michael Braun  <https://orcid.org/0000-0002-3961-6211>
Mohit Chatwani  <https://orcid.org/0009-0007-3471-6049>
Piyush Kumar  <https://orcid.org/0000-0002-8088-4672>
Ignacio Sanjuán  <https://orcid.org/0000-0002-5883-7095>
Ann Cathrin Brix  <https://orcid.org/0000-0002-5660-989X>
Dulce M Morales  <https://orcid.org/0000-0002-9420-2724>
Ulrich Hagemann  <https://orcid.org/0000-0002-1880-6550>
Markus Heidelmann  <https://orcid.org/0000-0002-6153-6103>
Justus Masa  <https://orcid.org/0000-0002-8555-5157>
Wolfgang Schuhmann  <https://orcid.org/0000-0003-2916-5223>
Corina Andronesco  <https://orcid.org/0000-0002-1227-1209>

References

- [1] Davis S J *et al* 2018 Net-zero emissions energy systems *Science* **360** eaas9793
- [2] Eryazici I, Ramesh N and Villa C 2021 Electrification of the chemical industry—materials innovations for a lower carbon future *MRS Bull.* **46** 1197–204
- [3] Seh Z W, Kibsgaard J, Dickens C F, Chorkendorff I, Nørskov J K and Jaramillo T F 2017 Combining theory and experiment in electrocatalysis: insights into materials design *Science* **355** eaad4998
- [4] Otto A, Robinius M, Grube T, Schiebahn S, Praktiknjo A and Stolten D 2017 Power-to-steel: reducing CO₂ through the integration of renewable energy and hydrogen into the German steel industry *Energies* **10** 451
- [5] Staffell I, Scamman D, Velazquez Abad A, Balcombe P, Dodds P E, Ekins P, Shah N and Ward K R 2019 The role of hydrogen and fuel cells in the global energy system *Energy Environ. Sci.* **12** 463–91
- [6] Liu K *et al* 2022 Electrocatalysis enabled transformation of earth-abundant water, nitrogen and carbon dioxide for a sustainable future *Mater. Adv.* **3** 1359–400
- [7] Luo Y, Zhang Z, Chhowalla M and Liu B 2022 Recent advances in design of electrocatalysts for high-current-density water splitting *Adv. Mater.* **34** e2108133
- [8] Suen N-T, Hung S-F, Quan Q, Zhang N, Xu Y-J and Chen H M 2017 Electrocatalysis for the oxygen evolution reaction: recent development and future perspectives *Chem. Soc. Rev.* **46** 337–65
- [9] Arshad F, Haq T U, Hussain I and Sher F 2021 Recent advances in electrocatalysts toward alcohol-assisted, energy-saving hydrogen production *ACS Appl. Energy Mater.* **4** 8685–701

- [10] Garlyyev B, Xue S, Fichtner J, Bandarenka A S and Andronesco C 2020 Prospects of value-added chemicals and hydrogen via electrolysis *ChemSusChem* **13** 2513–21
- [11] You B and Sun Y 2018 Innovative strategies for electrocatalytic water splitting *Acc. Chem. Res.* **51** 1571–80
- [12] Luque R, Herrero-Davila L, Campelo J M, Clark J H, Hidalgo J M, Luna D, Marinas J M and Romero A A 2008 Biofuels: a technological perspective *Energy Environ. Sci.* **1** 542
- [13] Rodionova M V, Poudyal R S, Tiwari I, Voloshin R A, Zharmukhamedov S K, Nam H G, Zayadan B K, Bruce B D, Hou H and Allakhverdiev S I 2017 Biofuel production: challenges and opportunities *Int. J. Hydrog. Energy* **42** 8450–61
- [14] Ciriminna R, Della Pina C, Rossi M and Pagliaro M 2014 Understanding the glycerol market *Eur. J. Lipid Sci. Technol.* **116** 1432–9
- [15] Alaba P A, Lee C S, Abnisa F, Aroua M K, Cognet P, Pérès Y and Wan Daud W M A 2020 A review of recent progress on electrocatalysts toward efficient glycerol electrooxidation *Rev. Chem. Eng.* **37** 116
- [16] Fan L, Liu B, Liu X, Senthilkumar N, Wang G and Wen Z 2020 Recent progress in electrocatalytic glycerol oxidation *Energy Technol.* **9** 2000804
- [17] Ramdin M et al 2019 High-pressure electrochemical reduction of CO₂ to formic acid/formate: effect of pH on the downstream separation process and economics *Ind. Eng. Chem. Res.* **58** 22718–40
- [18] Abdul Raman A A, Tan H W and Buthiyappan A 2019 Two-step purification of glycerol as a value added by product from the biodiesel production process *Front. Chem.* **7** 774
- [19] Kim Y et al 2017 The role of ruthenium on carbon-supported PtRu catalysts for electrocatalytic glycerol oxidation under acidic conditions *ChemCatChem* **9** 1683–90
- [20] Palma L M, Almeida T S, Morais C, Napporn T W, Kokoh K B and de Andrade A R 2017 Effect of co-catalyst on the selective electrooxidation of glycerol over ruthenium-based nanomaterials *ChemElectroChem* **4** 39–45
- [21] Velázquez-Hernández I, Álvarez-López A, Álvarez-Contreras L, Guerra-Balcázar M and Arjona N 2021 Electrocatalytic oxidation of crude glycerol from the biodiesel production on Pd-M (M = Ir, Ru or Pt) sub-10 nm nanomaterials *Appl. Surf. Sci.* **545** 149055
- [22] Zalineeva A, Serov A, Padilla M, Martínez U, Artyushkova K, Baranton S, Coutanceau C and Atanassov P 2015 Nano-structured Pd-Sn catalysts for alcohol electro-oxidation in alkaline medium *Electrochem. Commun.* **57** 48–51
- [23] Sandrini R M L M, Sempionatto J R, Tremiliosi-Filho G, Herrero E, Feliu J M, Souza-Garcia J and Angelucci C A 2019 Electrocatalytic oxidation of glycerol on platinum single crystals in alkaline media *ChemElectroChem* **6** 4238–45
- [24] Souza M B C D, Vicente R A, Yukuhiro V Y, V. M. T. Pires C T G, Cheuquepán W, J L B-N, Solla-Gullón J and Fernández P S 2019 Bi-modified Pt electrodes toward glycerol electrooxidation in alkaline solution: effects on activity and selectivity *ACS Catal.* **9** 5104–10
- [25] Li Z et al 2022 Alcohols electrooxidation coupled with H₂ production at high current densities promoted by a cooperative catalyst *Nat. Commun.* **13** 147
- [26] Zhang J, Liang Y, Li N, Li Z, Xu C and Jiang S P 2012 A remarkable activity of glycerol electrooxidation on gold in alkaline medium *Electrochim. Acta* **59** 156–9
- [27] Andreu T, Mallafre M, Molera M, Sarret M, Oriol R and Sirés I 2022 Effect of thermal treatment on nickel-cobalt electrocatalysts for glycerol oxidation *ChemElectroChem* **9** e202200100
- [28] Oliveira V L, Morais C, Servat K, Napporn T W, Tremiliosi-Filho G and Kokoh K B 2013 Glycerol oxidation on nickel based nanocatalysts in alkaline medium—identification of the reaction products *J. Electroanal. Chem.* **703** 56–62
- [29] Shilpa N, Pandikassala A, Krishnaraj P, Walko P S, Devi R N and Kurungot S 2022 Co-Ni layered double hydroxide for the electrocatalytic oxidation of organic molecules: an approach to lowering the overall cell voltage for the water splitting process *ACS Appl. Mater. Interfaces* **14** 16222–32
- [30] Song Y, Ji K, Duan H and Shao M 2021 Hydrogen production coupled with water and organic oxidation based on layered double hydroxides *Exploration* **1** 20210050
- [31] Martín-Yerga D, Henriksson G and Cornell A 2019 Effects of incorporated iron or cobalt on the ethanol oxidation activity of nickel (oxy)hydroxides in alkaline media *Electrocatalysis* **10** 489–98
- [32] Wang X et al 2020 Materializing efficient methanol oxidation via electron delocalization in nickel hydroxide nanoribbon *Nat. Commun.* **11** 4647
- [33] Wan H et al 2022 Electro-oxidation of glycerol to high-value-added C1–C3 products by iron-substituted spinel zinc cobalt oxides *ACS Appl. Mater. Interfaces* **14** 14293–301
- [34] Sun S, Sun L, Xi S, Du Y, Anu Prathap M U, Wang Z, Zhang Q, Fisher A and Xu Z J 2017 Electrochemical oxidation of C3 saturated alcohols on Co₃O₄ in alkaline *Electrochim. Acta* **228** 183–94
- [35] Ko T H, Devarayan K, Seo M K, Kim H Y and Kim B S 2016 Facile synthesis of core/shell-like NiCo₂O₄-decorated MWCNTs and its excellent electrocatalytic activity for methanol oxidation *Sci. Rep.* **6** 20313
- [36] Han X, Sheng H, Yu C, Walker T W, Huber G W, Qiu J and Jin S 2020 Electrocatalytic oxidation of glycerol to formic acid by CuCo₂O₄ spinel oxide nanostructure catalysts *ACS Catal.* **10** 6741–52
- [37] Dai L, Qin Q, Zhao X, Xu C, Hu C, Mo S, Wang Y O, Lin S, Tang Z and Zheng N 2016 Electrochemical partial reforming of ethanol into ethyl acetate using ultrathin Co₃O₄ nanosheets as a highly selective anode catalyst *ACS Cent. Sci.* **2** 538–44
- [38] Santiago P V, Lima C C, Bott-Neto J L, Fernández P S, Angelucci C A and Souza-Garcia J 2021 Perovskite oxides as electrocatalyst for glycerol oxidation *J. Electroanal. Chem.* **896** 115198
- [39] Brix A C et al 2022 Structure-performance relationship of LaFe_{1-x}Co_xO₃ electrocatalysts for oxygen evolution, isopropanol oxidation, and glycerol oxidation *ChemElectroChem* **9** e202200092
- [40] Morales D M, Jambrec D, Kazakova M A, Braun M, Sikdar N, Koul A, Brix A C, Seisel S, Andronesco C and Schuhmann W 2022 Electrocatalytic conversion of glycerol to oxalate on Ni oxide nanoparticles-modified oxidized multiwalled carbon nanotubes *ACS Catal.* **12** 982–92
- [41] Stitz A and Buchberger W 1994 Studies on electrochemical reactions at metal-oxide electrodes for combination with high-performance liquid chromatography *Electroanalysis* **6** 251–8
- [42] Yu X, Araujo R B, Qiu Z, Campos Dos Santos E, Anil A, Cornell A, Pettersson L G M and Johansson M 2022 Hydrogen evolution linked to selective oxidation of glycerol over CoMoO₄—a theoretically predicted catalyst *Adv. Energy Mater.* **12** 2103750
- [43] Li J, Luo F, Zhao Q, Xiao L, Yang J, Liu W and Xiao D 2019 Crystalline nickel boride nanoparticle agglomerates for enhanced electrocatalytic methanol oxidation *Int. J. Hydrog. Energy* **44** 23074–80
- [44] Cychy S, Lechler S and Muhler M 2022 Selective anodic oxidation of solketal as acetal-protected glycerol over nickel boride in alkaline media to glyceric acid *ChemElectroChem* **9** e202101214
- [45] Barwe S, Weidner J, Cychy S, Morales D M, Dieckhöfer S, Hiltrop D, Masa J, Muhler M and Schuhmann W 2018 Electrocatalytic oxidation of 5-(hydroxymethyl)furfural using high-surface-area nickel boride *Angew. Chem., Int. Ed.* **57** 11460–4

- [46] Brix A C *et al* 2021 Electrocatalytic oxidation of glycerol using solid-state synthesised nickel boride: impact of key electrolysis parameters on product selectivity *ChemElectroChem* **8** 2336–42
- [47] Cychy S, Lechler S, Huang Z, Braun M, Brix A C, Blümler P, Andronesu C, Schmid F, Schuhmann W and Muhler M 2021 Optimizing the nickel boride layer thickness in a spectroelectrochemical ATR-FTIR thin-film flow cell applied in glycerol oxidation *Chin. J. Catal.* **42** 2206–15
- [48] Zhang J, Li X, Liu Y, Zeng Z, Cheng X, Wang Y, Tu W and Pan M 2018 Bi-metallic boride electrocatalysts with enhanced activity for the oxygen evolution reaction *Nanoscale* **10** 11997–2002
- [49] Xu N, Cao G, Chen Z, Kang Q, Dai H and Wang P 2017 Cobalt nickel boride as an active electrocatalyst for water splitting *J. Mater. Chem. A* **5** 12379–84
- [50] Sun J, Zhang W, Wang S, Ren Y, Liu Q, Sun Y, Tang L, Guo J and Zhang X 2019 Ni-Co-B nanosheets coupled with reduced graphene oxide towards enhanced electrochemical oxygen evolution *J. Alloys Compd.* **776** 511–8
- [51] He T, Nsanzimana J M V, Qi R, Zhang J-Y, Miao M, Yan Y, Qi K, Liu H and Xia B Y 2018 Synthesis of amorphous boride nanosheets by the chemical reduction of Prussian blue analogs for efficient water electrolysis *J. Mater. Chem. A* **6** 23289–94
- [52] Li Y *et al* 2019 Multimetal borides nanochains as efficient electrocatalysts for overall water splitting *Small* **15** e1804212
- [53] Wang S, He P, Xie Z, Jia L, He M, Zhang X, Dong F, Liu H, Zhang Y and Li C 2019 Tunable nanocotton-like amorphous ternary Ni-Co-B: a highly efficient catalyst for enhanced oxygen evolution reaction *Electrochim. Acta* **296** 644–52
- [54] Andronesu C, Barwe S, Ventosa E, Masa J, Vasile E, Konkana B, Möller S and Schuhmann W 2017 Powder catalyst fixation for post-electrolysis structural characterization of NiFe layered double hydroxide based oxygen evolution reaction electrocatalysts *Angew. Chem., Int. Ed.* **56** 11258–62
- [55] Barwe S, Andronesu C, Masa J, Ventosa E, Klink S, Genç A, Arbiol J and Schuhmann W 2017 Polybenzoxazine-derived N-doped carbon as matrix for powder-based electrocatalysts *ChemSusChem* **10** 2653–9
- [56] Möller S, Barwe S, Dieckhöfer S, Masa J, Andronesu C and Schuhmann W 2020 Differentiation between carbon corrosion and oxygen evolution catalyzed by NiB/C hybrid electrocatalysts in alkaline solution using differential electrochemical mass spectrometry *ChemElectroChem* **7** 2680–6
- [57] Barwe S, Andronesu C, Engels R, Conzuelo F, Seisel S, Wilde P, Chen Y-T, Masa J and Schuhmann W 2019 Cobalt metalloid and polybenzoxazine derived composites for bifunctional oxygen electrocatalysis *Electrochim. Acta* **297** 1042–51
- [58] Chanda V, Junqueira J R C, Sikdar N, Sanjuán I, Braun M, Dieckhöfer S, Seisel S and Andronesu C 2022 A CuOx/Cu/C electrocatalyst-based gas diffusion electrode for the electroreduction of CO₂ with high selectivity to C₂H₄ *Electrochem. Sci. Adv.* e2100200
- [59] Masa J, Sinev I, Mistry H, Ventosa E, La Mata M D, Arbiol J, Muhler M, Roldan C B and Schuhmann W 2017 Ultrathin high surface area nickel boride (Ni_xB) nanosheets as highly efficient electrocatalyst for oxygen evolution *Adv. Energy Mater.* **7** 1700381
- [60] Masa J, Weide P, Peeters D, Sinev I, Xia W, Sun Z, Somsen C, Muhler M and Schuhmann W 2016 Amorphous cobalt boride (Co₂B) as a highly efficient nonprecious catalyst for electrochemical water splitting: oxygen and hydrogen evolution *Adv. Energy Mater.* **6** 1502313
- [61] Moulder J F, Stickle W F, Sobol P E, Bomben K D and King Jr R C 1992 *Handbook of X-Ray Photoelectron Spectroscopy: A Reference Book of Standard Spectra for Identification and Interpretation of XPS Data* (Eden Prairie: Physical Electronics)
- [62] Knobel M 1923 The activities of the ions of potassium hydroxide in aqueous solution *J. Am. Chem. Soc.* **45** 70–76
- [63] Hamer W J and Wu Y-C 1972 Osmotic coefficients and mean activity coefficients of uni-univalent electrolytes in water at 25 °C *J. Phys. Chem. Ref. Data* **1** 1047–100
- [64] Bromley L A 1973 Thermodynamic properties of strong electrolytes in aqueous solutions *AIChE J.* **19** 313–20
- [65] Morales D M and Risch M 2021 Seven steps to reliable cyclic voltammetry measurements for the determination of double layer capacitance *J. Phys. Energy* **3** 34013
- [66] McCrory C C L, Jung S, Peters J C and Jaramillo T F 2013 Benchmarking heterogeneous electrocatalysts for the oxygen evolution reaction *J. Am. Chem. Soc.* **135** 16977–87
- [67] Braun M *et al* 2022 Electrooxidation of alcohols on mixed copper-cobalt hydroxycarbonates in alkaline solution *ChemElectroChem* **9** e202200267
- [68] Radha A V, Weiß S, Sanjuán I, Ertl M, Andronesu C and Breu J 2021 The effect of interlayer anion grafting on water oxidation electrocatalysis: a comparative study of Ni- and Co-based brucite-type layered hydroxides, layered double hydroxides and hydroxynitrate salts *Chem. Eur. J.* **27** 16930–7
- [69] Geng J, Jefferson D A and Johnson B F G 2007 The unusual nanostructure of nickel-boron catalyst *Chem. Commun.* 969–71
- [70] Careno S, Portehault D, Boissière C, Mézailles N and Sanchez C 2013 Nanoscaled metal borides and phosphides: recent developments and perspectives *Chem. Rev.* **113** 7981–8065
- [71] Biesinger M C, Payne B P, Grosvenor A P, Lau L W, Gerson A R and Smart R S 2011 Resolving surface chemical states in XPS analysis of first row transition metals, oxides and hydroxides: Cr, Mn, Fe, Co and Ni *Appl. Surf. Sci.* **257** 2717–30
- [72] Demirci U B and Miele P 2010 Cobalt in NaBH₄ hydrolysis *Phys. Chem. Chem. Phys.* **12** 14651–65
- [73] Rabe A *et al* 2021 The roles of composition and mesostructure of cobalt-based spinel catalysts in oxygen evolution reactions *Chem. Eur. J.* **27** 17038–48
- [74] Osaka T, Iwase Y, Kitayama H and Ichino T 1983 Oxygen evolution reaction on composite cobalt borides *Bull. Chem. Soc. Jpn.* **56** 2106–11
- [75] Ghosh S, Mondal B, Roy S, Shalom M and Sadan M B 2022 Alcohol oxidation with high efficiency and selectivity by nickel phosphide phases *J. Mater. Chem. A* **10** 8238–44
- [76] Kwon Y, Lai S C S, Rodriguez P and Koper M T M 2011 Electrocatalytic oxidation of alcohols on gold in alkaline media: base or gold catalysis? *J. Am. Chem. Soc.* **133** 6914–7
- [77] Nwabara U O, Hernandez A D, Henckel D A, Chen X, Cofell E R, De-heer M P, Verma S, Gewirth A A and Kenis P J A 2021 Binder-focused approaches to improve the stability of cathodes for CO₂ electroreduction *ACS Appl. Energy Mater.* **4** 5175–86
- [78] Li G-F, Yang D and Abel Chuang P-Y 2018 Defining nafion ionomer roles for enhancing alkaline oxygen evolution electrocatalysis *ACS Catal.* **8** 11688–98
- [79] Yang F, Xin L, Uzunoglu A, Qiu Y, Stanciu L, Ilavsky J, Li W and Xie J 2017 Investigation of the interaction between Nafion ionomer and surface functionalized carbon black using both ultrasmall angle x-ray scattering and cryo-TEM *ACS Appl. Mater. Interfaces* **9** 6530–8
- [80] Berlinger S A, McCloskey B D and Weber A Z 2021 Probing ionomer interactions with electrocatalyst particles in solution *ACS Energy Lett.* **6** 2275–82
- [81] Holdcroft S 2014 Fuel cell catalyst layers: a polymer science perspective *Chem. Mater.* **26** 381–93